ADVANCED INTELLIGENT SYSTEMS
Open Access
www.advintellsyst.com

Design and Optimization of a Magnetic Field Generator for Magnetic Particle Imaging with Soft Magnetic Materials

Fynn Foerger, Marija Boberg, Jonas Faltinath, Tobias Knopp, and Martin Möddel*

Magnetic field generators are a key component of Magnetic Particle Imaging (MPI) systems, and their power consumption is a major obstacle on the path to human-sized scanners. Despite their importance, a focused discussion of these generators is rare, and a comprehensive description of the design process is currently lacking. This work presents a methodology for the design and optimization of selection field generators operating with soft magnetic materials outside the linear regime in the context of MPI. Key elements are a mathematical model of magnetic field generators, a formalism for defining field sequences, and a relationship between power consumption and field sequence. These are used to define the design space of a field generator given its system requirements and constraints. The design process is then formulated as an optimization problem. Subsequently, this methodology is then utilized to design a new magnetic field generator specifically for cerebral imaging studies. The optimization result outperforms our existing MPI field generator in terms of power consumption and field of view size, providing a proof-of-concept for the entire methodology. As the approach is very general, it can be extended beyond the MPI context to other areas such as magnetic manipulation of medical devices and micro-robotics.

1. Introduction

Magnetic fields have become an indispensable part of modern medicine. Their ability to penetrate the human body harmlessly and interact with tissues and materials in an adjustable manner makes them a valuable tool in medical diagnosis and intervention. A significant portion of medical magnetic field applications are centered around tomographic imaging.[1] Examples include magnetic resonance imaging,[2,3] or magnetic particle imaging (MPI).[4,5] In addition, magnetic forces and torques are used in a variety of medical applications, such as precise surgery, targeted drug delivery, or medical examination,[6] e.g. actuation of magnetic microrobots,[7,8] or catheter guidance.[9,10]

Each application necessitates the precise generation of specific magnetic fields, which is done by magnetic field generators. Depending on the specific application it may be necessary to generate fields with high homogeneity, a certain strength or spatial profile. These requirements are also reflected in the generator design.[11] When designing the generator, it is important to ensure that it is able to generate the desired magnetic fields while meeting other requirements, such as upper limiton power consumption, weight, or price. The related process is an optimization problem with a high-dimensional design space. In practice, the identification of an optimal solution for the specific application domain can be challenging due to nonlinear dependencies.

In the macroscopic regime magnetic fields can be generated by currents or hard and soft magnetic materials. In practice this involves the use of current-carrying coils[12] or permanent magnets.[13] This work considers a special form of current-carrying coils: coils that amplify magnetic fields with inbuilt soft magnetic materials. Compared to air coils, this significantly reduces the power consumption for a given field.[14,15] Such coils allow precise field adjustment and are suitable for applications with flexible and high field strengths while keeping mechanical effort and infrastructure requirements low. The use of soft iron for field enhancement in static magnetic fields is a very promising approach, especially in the MPI field, as the demands on field homogeneity are not as high compared to other imaging modalities. Despite of this fact, the use of soft iron to generate quasi-static magnetic fields is a rarely discussed topic. For coils in Maxwell configuration, which are mainly operated in the linear range, Le et al. present a geometry optimization where the gradient in the center of the structure is maximized.[16,17] Additionally, Bontus et al. describe a selection field optimization for the current density along the coils for their soft iron selection

F. Foerger, M. Boberg, J. Faltinath, T. Knopp, M. Möddel
Institute for Biomedical Imaging
Hamburg University of Technology
22529 Hamburg, Germany
E-mail: fynn.foerger@tuhh.de

F. Foerger, M. Boberg, J. Faltinath, T. Knopp, M. Möddel
Section for Biomedical Imaging
University Medical Center Hamburg-Eppendorf
22529 Hamburg, Germany

The ORCID identification number(s) for the author(s) of this article can be found under https://doi.org/10.1002/aisy.202400017.

DOI: 10.1002/aisy.202400017

field generator.[15] A linear relationship between current and field is assumed, for both generators. A comprehensive description of the interplay between generatable field sequences and the field generator optimization process involving nonlinearities due to saturation effects is still lacking.

MPI is a tracer-based tomography technique that uses static gradient fields with a low-field region along with dynamic excitation fields to image the concentration of iron nanoparticles.[12,18,19] Various sizes of magnetic field generators have been incorporated into MPI systems, over the past two decades. First preclinical MPI systems had bore sizes of up to 12 cm and gradient strengths of up to $3.4\,\mathrm{Tm}^{-1}$.[12,20] Subsequently, researchers have been working on scaling up the MPI systems to the clinical scale.[15,21] The torso-scale system used soft iron to amplify the fields, which was a novelty in MPI.[21] They could reach a gradient of $2\,\mathrm{Tm}^{-1}$ covering a workspace of 20 cm. In addition to increasing the field of view, researchers have focused on several other capabilities of the field generator, such as high gradient strengths of up to $7\,\mathrm{Tm}^{-1}$,[22] field-free line (FFL) topologies,[23–25] and traveling-wave sequences.[26,27]

On the way to human-scale MPI scanners, the power consumption of a system is a major obstacle as it is increasingly difficult to generate sufficiently large fields. Naturally, the reduction of power consumption is of great significance. With conventional MPI scanners, most of the power is required to generate the static magnetic fields. Accordingly, this part of a scanner also holds great potential for improvements.

The magnetic fields used for MPI in its standard configuration are very similar to the fields needed to apply forces or torques for micromanipulation of magnetic devices or particles. As MPI magnetic field generators have evolved, so have field generators that are dedicated solely to magnetic actuation. Some of the systems use paired coils in Helmholtz and Maxwell configurations to generate homogeneous and gradient fields.[28–31] To improve energy efficiency and reduce layout restrictions, actuation systems with distributed electromagnets were developed.[6] Many of these systems utilize soft magnetic materials for field amplification and come with different number of coils and orientations.[32–34] Future research in this area will also focus on the creation of useful strategies for the targeted generation of magnetic field gradients in 3D.[8]

Due to the similarity in the field generation requirements for MPI and flexible magnetic actuation, it is possible to combine both approaches in an electromagnetic actuation system with imaging capabilities that offers the potential for magnetic manipulation supported by real-time spatial feedback from inside the human body.[10,21,35,36] This article describes the design process of such a generator for MPI brain imaging. An optimization problem is derived from the various requirements, which is then solved by a grid search. The optimization process leads to a design consisting of a total of 18 coils with a soft iron core arranged in coil arrays and an enclosing iron coating. This generator is not only more efficient in terms of power consumption than previous ones, but can also generate very flexible magnetic fields due to the large number of coils, allowing it to be used in a variety of magnetic applications.

2. Theory

To develop a power-optimized magnetic field generator for MPI using soft magnetic materials, this section will introduce the concepts and tools necessary to achieve this goal. To do so, we will explain what magnetic fields are used in MPI and which types of measurement sequences (field sequences) are required for imaging with a large field of view. The order of the sequences in this work defines a set hierarchy, whereby each field sequence extension contains the previous field sequences. We will define magnetic field generators and introduce the inverse current problem, i.e. which input currents of a field generator realize given measurement sequences. Using these methods, we can then formulate the search for a power-optimized magnetic field generator for MPI as an optimization problem, the solution of which we approximate for our specific requirements and some simplifications in the following sections. Note that the section is kept as general as possible so that the approach can also be applied to power optimization of field generator designs outside the MPI context.

2.1. Signal Generation and Encoding in MPI

To lay a foundation, the basic principles of signal generation and spatial encoding in MPI are discussed next. A comprehensive discussion of the imaging fundamentals in the field of MPI can be found in refs. [4,37,38].

MPI is a tracer-based imaging modality in which the concentration of administered tracers within the bloodstream is determined. The tracer material consists of magnetic nanoparticles that are constantly remagnetized in an alternating magnetic field. Due to the nonlinear relationship between the particle magnetization and the exciting field, harmonics of the exciting fundamental frequency are generated by the tracer. These harmonics can be measured and used to infer the tracer concentration.

2.1.1. General MPI Setting

Generating tomographic images of the tracer distribution requires knowledge of the relationship between the MPI measurement signal $\boldsymbol{v}:\mathbb{T}\to\mathbb{R}^L$ in the time interval $\mathbb{T}=[0,T]$ and the tracer concentration $c:\Omega\to\mathbb{R}_0^+$. Here, $T\in\mathbb{R}_0^+$ is the duration of a measurement cycle and L is the number of receive channels. For our purposes, we use the general mathematical model of the MPI signal equation

$$v_l(t) = -\int_\Omega c(\boldsymbol{r})\boldsymbol{s}_l(\boldsymbol{r},\tau)d\boldsymbol{r} \tag{1}$$

where $\Omega\subseteq\mathbb{R}^3$ is the field of view of the MPI system and $l\in\{1,\ldots,L\}$. The system function $\boldsymbol{s}:\Omega\times\mathbb{T}\to\mathbb{R}^L$

$$\boldsymbol{s}_l(\boldsymbol{r},t) = \mu_0\int_{\mathbb{T}}\tilde{a}_l(t-\tau)\left\langle \boldsymbol{p}(\boldsymbol{r}),\quad \frac{\partial}{\partial t}\boldsymbol{m}(\boldsymbol{B}_{\mathrm{app}}(\boldsymbol{r},t),t)\right\rangle d\tau \tag{2}$$

describes the system response of an MPI tracer to an applied magnetic field $\boldsymbol{B}_{\mathrm{app}}:\Omega\times\mathbb{T}\to\mathbb{R}^3$, where $\boldsymbol{p}:\Omega\to\mathbb{R}^L$ is the receive coil sensitivity, $\boldsymbol{m}:\Omega\times\mathbb{T}\to\mathbb{R}^3$ is the magnetization of the

particle ensemble, and μ_0 is the vacuum permeability (the physically correct term for $\boldsymbol{B}_{\text{app}}$ would be magnetic flux density. For the sake of readability, the magnetic flux density is referred to as the magnetic field as long as it is considered in a region of space where they differ only by the factor μ_0).[38] $\tilde{\boldsymbol{a}}: \mathbb{T} \to \mathbb{R}^L$ are the periodic kernel functions associated to receive chain components like the low noise amplifiers or the analogue filters, which dampen the direct feed through signal.

The temporal and spatial variation of the applied magnetic field during an imaging cycle is referred to as the magnetic field sequence and is responsible for the generation and spatial encoding of the magnetization signal.[12] The magnetic field sequences must be chosen in such a way that the system function is a suitable base set from which high-resolution image reconstruction can be performed.[39] In general, the applied field is composed of two different parts

$$\boldsymbol{B}_{\text{app}}(\boldsymbol{r}, t) = \boldsymbol{B}_{\text{sf}}(\boldsymbol{r}, t) + \boldsymbol{B}_{\text{df}}(\boldsymbol{r}, t) \tag{3}$$

A selection field $\boldsymbol{B}_{\text{sf}}: \Omega \times \mathbb{T} \to \mathbb{R}^3$, whose slew rate is small, such that no significant change in magnetization is induced and which is responsible for the spatial coding of the particle distribution into the measurement signal. In contrast, the drive field $\boldsymbol{B}_{\text{df}}: \Omega \times \mathbb{T} \to \mathbb{R}^3$ is rapidly changing at fast slew rates generating the main part of the measurement signal. In practice, the drive fields are limited in frequency and amplitude by hardware and medical constraints. The latter is the specific absorption rate (SAR) in tissue and peripheral nerve stimulation (PNS).[40–42]

2.1.2. Ideal Single-Patch Sequences

The ideal single-patch sequence describes the simple textbook MPI field sequence, where selection fields are explicitly time independent. In a first-order Taylor expansion with the expansion point $\tilde{\boldsymbol{r}} \in \Omega$, the ideal MPI selection field is given by

$$\boldsymbol{B}_{\text{sf}}(\boldsymbol{r}) = \boldsymbol{B}_{\text{sf}}\Big|_{\tilde{\boldsymbol{r}}} + \sum_{i \in \{x,y,z\}} \frac{\partial \boldsymbol{B}_{\text{sf}}}{\partial r_i}\Big|_{\tilde{\boldsymbol{r}}} (r_i - \tilde{r}_i) \tag{4}$$

$$=: \boldsymbol{B}_{\tilde{\boldsymbol{r}}} + \boldsymbol{J}_{\tilde{\boldsymbol{r}}}(\boldsymbol{r} - \tilde{\boldsymbol{r}}) \tag{5}$$

where $\boldsymbol{B}_{\tilde{\boldsymbol{r}}}$ is the offset field at the expansion point $\tilde{\boldsymbol{r}}$ and the Jacobian matrix.

$$\boldsymbol{J}_{\tilde{\boldsymbol{r}}} = \text{diag}(G_x, G_y, G_z) \tag{6}$$

is diagonal and time independent. Its diagonal entries $G_x, G_y, G_z \in \mathbb{R}$ are referred to as the gradient strengths in the MPI context and are the key parameters determining the spatial resolution of an MPI system.[12,39] Due to the source free nature of the magnetic field, it holds that $G_x + G_y + G_z = 0$. The stronger the gradient strengths, the better the spatial resolution. If $\boldsymbol{J}_{\tilde{\boldsymbol{r}}}$ is nonsingular, the field has a characteristic field-free point (FFP). Otherwise if $\boldsymbol{J}_{\tilde{\boldsymbol{r}}} = 0$ but singular, it has a characteristic FFL.

In an ideal setup, the selection field is often combined with homogeneous drive fields of the form

$$\boldsymbol{B}_{\text{df}}(\boldsymbol{r}, t) = \begin{pmatrix} b_x \sin(2\pi f_x t + \varphi_x) \\ b_y \sin\left(2\pi f_y t + \varphi_y\right) \\ b_z \sin(2\pi f_z t + \varphi_z) \end{pmatrix} \tag{7}$$

where $b_x, b_y, b_z \in \mathbb{R}$ are the drive field amplitudes, f_x, f_y, and $f_z \in \mathbb{R}$ are the excitation frequencies, and $\varphi_x, \varphi_y, \varphi_z \in \mathbb{R}$ are the phase shifts of the excitation. If amplitudes and frequencies are nonzero and the frequencies have pairwise rational ratios the FFP or FFL or in general, the field-free region (FFR) moves along a 3D Lissajous trajectory. Under these conditions the field of view of an FFP scanner can be specified by a cube of size

$$\frac{2b_x}{G_x} \times \frac{2b_y}{G_y} \times \frac{2b_z}{G_z} \tag{8}$$

Typically, it is several cubic centimeters in size,[43] which is also referred to as patch in the MPI context. Note that there are also other typical excitation types where one or two of the amplitudes are zero. In these cases the FFR moves on a 2D Lissajous trajectory or line, respectively.

2.1.3. Focus-Field-Based Multi-Patch Sequences

The ideal single-patch sequences described so far are characterized by homogeneous magnetic excitation fields $\boldsymbol{B}_{\text{df}}$ and a static selection field $\boldsymbol{B}_{\text{sf}}$. For imaging larger volumes, a focus field similar to the drive field but at a lower frequency can be used to shift a single patch[44] either step by step[18] or continuously[19] through a larger volume while keeping the excitation field unchanged.[12] This allows to slowly shift the patch described earlier and in turn extends the field of view of the imaging system while complying to PNS and SAR limits. The described sequence or variations of it have been implemented numerous times under various names, including large field of view,[18,44] partial field of view,[45] axially elongated data acquisition,[46] traveling wave,[26] and multi-patch.[47]

These sequences can be modeled by introducing a time-dependent offset field $\boldsymbol{B}_{\tilde{\boldsymbol{r}}}(t)$ which results in a time-dependent selection field.

$$\boldsymbol{B}_{\text{sf}}(\boldsymbol{r}, t) = \boldsymbol{B}_{\tilde{\boldsymbol{r}}}(t) + \boldsymbol{J}_{\tilde{\boldsymbol{r}}}(\boldsymbol{r} - \tilde{\boldsymbol{r}}) \tag{9}$$

The linear relationship between the offset field and the position of the patch makes it comparatively easy to plan measurement sequences, predict the resulting field of view, and calculate the required field sequences. Moreover, it allows to simplify image reconstruction insofar as the measurement sequence does not have to be considered as a whole, but can be divided into smaller parts, which drastically reduces the numerical complexity of the reconstruction problem.[47,48] Similarly, it allows the x-space imaging method[49] to extend the field of view.[45]

2.1.4. Dynamic Gradient-Based Multi-Patch Sequences

Another starting point for manipulating imaging sequences is the gradient field. It is determined by the Jacobian matrix $\boldsymbol{J}_{\tilde{\boldsymbol{r}}}$, which so far we have assumed to be static and diagonal. If we ease these restrictions, we obtain gradient fields which can be

described by time-dependent and not necessarily diagonal Jacobian matrices.

$$\boldsymbol{B}_{\mathrm{sf}}(\boldsymbol{r},t) = \boldsymbol{B}_{\tilde{\boldsymbol{r}}}(t) + \boldsymbol{J}_{\tilde{\boldsymbol{r}}}(t)(\boldsymbol{r}-\tilde{\boldsymbol{r}}) \tag{10}$$

The set of dynamic gradient-based multi-patch sequences allows, for example, to vary the spatial resolution by adjusting the gradient strength.[50] These sequences are of even greater importance for MPI systems with an FFL topology, since a rotation of the FFL can generate computed tomographie-like projection data.[23] The images can then be reconstructed with the filtered back projection.[51] In addition, with certain coil geometries, it can be more power efficient to generate these sheared and possibly rotated magnetic fields compared to the ideal gradient fields from the previous sections.

In this more general scenario the diagonal entries of $\boldsymbol{J}_{\tilde{\boldsymbol{r}}}(t)$ can no longer be used to characterize the gradient strengths. As a consequence of Maxwell's equations in the absence of current densities in the bore of an MPI system ($\nabla \times \boldsymbol{B} = \boldsymbol{0}$), the Jacobian matrix is square and symmetric. Therefore, it can be factorized by an eigenvalue decomposition $\boldsymbol{J}_{\tilde{\boldsymbol{r}}}(t) = \boldsymbol{Q}(t)\boldsymbol{\Lambda}(t)\boldsymbol{Q}^{-1}(t)$ into a diagonal matrix $\boldsymbol{\Lambda}(t)$ whose diagonal elements are the corresponding eigenvalues $\lambda_i(t)$ of $\boldsymbol{J}_{\tilde{\boldsymbol{r}}}(t)$ and a square matrix $\boldsymbol{Q}(t)$ whose columns are the corresponding eigenvectors. For later use, the eigenvalues are sorted by their absolute value: $|\lambda_1(t)| \geq |\lambda_2(t)| \geq |\lambda_3(t)|$. This decomposition allows us to generalize the characterization via the gradient strengths used so far.[15] The eigenvalues take the role of the gradient strengths and the eigenvectors inform us about the direction in which the gradient strength is applied. Similar to G_x, G_y, G_z in Equation (6), it also applies to the generalized gradient strengths that $\lambda_1(t) + \lambda_2(t) + \lambda_3(t) = 0$ due to $\nabla \boldsymbol{B} = 0$.

2.1.5. General Multi-Patch Sequences

All sequences presented so far have in common that they were based on ideal fields. These are magnetic fields which consist at least in good approximation of homogeneous magnetic fields, ideal gradient fields, or a superposition of them. MPI multi-patch measurement sequences, which operate with selection fields that do not meet these requirements, are classified as general multi-patch measurement sequences and can be represented by additional terms of higher order with potentially time-dependent coefficients

$$\begin{aligned}\boldsymbol{B}_{\mathrm{sf}}(\boldsymbol{r},t) = \boldsymbol{B}_{\tilde{\boldsymbol{r}}}(t) + \boldsymbol{J}_{\tilde{\boldsymbol{r}}}(t)(\boldsymbol{r}-\tilde{\boldsymbol{r}}) \\ + \sum_{i\in\{x,y,z\}}\sum_{k\in\{x,y,z\}} \left.\frac{\partial^2 \boldsymbol{B}_{\mathrm{sf}}(\cdot,t)}{\partial r_i \partial r_k}\right|_{\tilde{\boldsymbol{r}}} (r_i-\tilde{r}_i)(r_k-\tilde{r}_k) \\ + \dots .\end{aligned} \tag{11}$$

They are the most generalized field sequences and contain all previous field sequences, due to the hierarchical structure of the field sequence definitions. As a direct consequence of the nonlinearity of the selection field, the relationship between the offset field and the position of the FFR also becomes nonlinear. In addition, such a selection field will generally have locally varying spatial resolutions, since a change in the expansion point leads to a change in the Jacobian matrix. Considering only the previous field models, this effect is not observed in the selection fields. It makes it more difficult to plan measurement sequences, predict the resulting field of view and resolution, and calculate the required field sequence. In addition, the nonlinearities can lead to image distortions if they are neglected in imaging or image reconstruction.[48,52] **Figure 1** shows a comparison of all the field sequences presented here using the example of an FFL.

Despite these difficulties, general multi-patch sequences offer great potential by liberating MPI system designers from the rigid corset of implementing ideal magnetic fields. For example, it is conceivable to design multi-patch sequences in which the Jacobian matrix along an FFR trajectory does not have a specific reference matrix as a target but rather requirements on the eigenvalues or eigenvectors that ensure a certain spatial resolution or orientation. The additional degrees of freedom provided by such an approach could then be used to achieve other goals, such as minimizing the power consumption of the selection field generators. Then during a sequence, the direction of the strongest and weakest field change would vary. This however, does not pose a problem for the system matrix-based image reconstruction or the image quality, as these field changes would be encoded in the previously recorded system matrix. The focus of this work is to explicitly use this field description to design a new type of selection field generator. This is an optimization problem in which a choice must be made from the large space of all possible field generation methods and designs.

2.2. Field Generator

There are various approaches for generating magnetic fields. These can be created using current density carrying conductors or hard magnetic materials, and amplified and deformed using soft magnetic materials. These parts are arranged in a particular configuration $\delta \in \Delta$ from the infinite set of possible configurations Δ with $N \in \mathbb{N}$ individually driven coils. At this level of abstraction, the corresponding field generator has N time-dependent continuous input currents $\tilde{\boldsymbol{I}} \in \mathcal{C}^1(\mathbb{T},\mathbb{R}^N)$ which cause a configuration-dependent distribution of current densities. These in turn generate a time-dependent twofold continuously differentiable magnetic field $\tilde{\boldsymbol{B}}_{\delta,\tilde{I}} \in \mathcal{C}^2(\Omega\times\mathbb{T},\mathbb{R}^3)$. As such, we can describe a field generator via a mapping from input currents to magnetic fields

$$\tilde{\mathcal{G}}_\delta : \mathcal{C}^0(\mathbb{T},\mathbb{R}^N) \to \mathcal{C}^2(\Omega\times\mathbb{T},\mathbb{R}^3), \quad \tilde{\mathcal{G}}_\delta(\tilde{\boldsymbol{I}}) = \tilde{\boldsymbol{B}}_{\delta,\tilde{I}} \tag{12}$$

In this article, we consider field generators that use a combination of coils and soft magnetic materials to generate magnetic fields. The coils are driven at low slew rates such that the magnetic field $\boldsymbol{B}_{\delta,I} \in \mathcal{C}^2(\Omega,\mathbb{R}^3)$ generated at time $t \in \mathbb{R}$ only depends on the present input current $\boldsymbol{I} \in \mathbb{R}^N$. In this scenario, a field generator is described by the mapping.

$$\mathcal{G}_\delta : \mathbb{R}^N \to \mathcal{C}^2(\Omega,\mathbb{R}^3), \quad \mathcal{G}_\delta(\boldsymbol{I}) = \boldsymbol{B}_{\delta,I} \tag{13}$$

The mappings Equation (12) and (13) are related via the time projection mappings for the current $\Pi_{\mathrm{c},t} : \mathcal{C}^0(\mathbb{T},\mathbb{R}^N) \to \mathbb{R}^N$, $\tilde{\boldsymbol{I}} \mapsto \tilde{\boldsymbol{I}}(t) = \boldsymbol{I}$ and for the field $\Pi_{\mathrm{f},t} : \mathcal{C}^2(\Omega\times\mathbb{T},\mathbb{R}^3) \to \mathcal{C}^2(\Omega,\mathbb{R}^3)$, $\tilde{\boldsymbol{B}}_{\delta,\tilde{I}} \mapsto \tilde{\boldsymbol{B}}_{\delta,\tilde{I}(t)}(\,\cdot\,,t) = \boldsymbol{B}_{\delta,I}$ by the following commutative diagram:

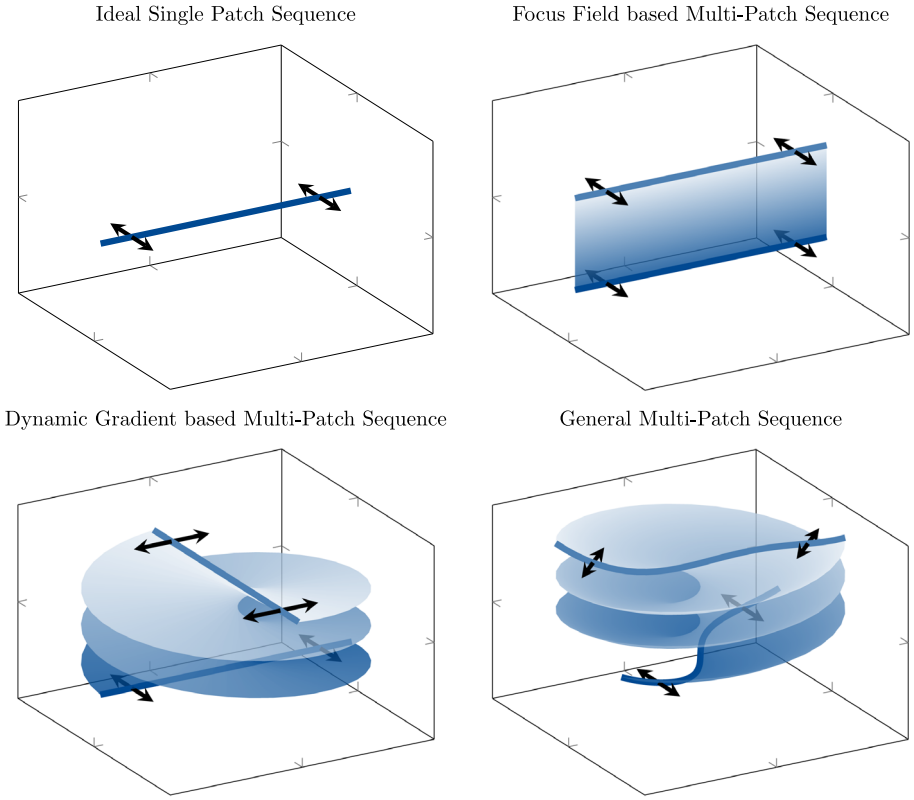

Figure 1. Comparison of different field sequences. The previously defined field sequences are illustrated in this example using an FFL topology. Blue lines indicate the start and end positions of the FFL of $\boldsymbol{B}_{\text{sf}}$ at the beginning and end of the sequence. The light to dark-blue-shaded surface represents the trajectory of the FFL and the black arrows show the direction of the FFL motion due to the drive field $\boldsymbol{B}_{\text{df}}$. In the ideal single-patch sequence the FFL can only be moved in time through the drive field. If homogeneous offset fields are added, this is referred to as a focus-field-based multi-patch sequence. As a result, a linear displacement of the field-free region is possible. With dynamic-gradient-based multi-patch sequences a change in the Jacobian matrix is also permitted, which allows sequences with rotating FFLs, for example. The most general type of sequence allows higher order terms in the selection field. These sequences are called general multi-patch sequences. Thus, the shape of the field-free region may deviate from the ideal, potentially leading to the formation of curved lines or multiple FFPs.

$$\begin{array}{ccc} \mathcal{C}^0(\mathbb{T},\mathbb{R}^N) & \xrightarrow{\tilde{\mathcal{G}}_\delta} & \mathcal{C}^2(\Omega\times\mathbb{T},\mathbb{R}^3) \\ \downarrow{\scriptstyle \Pi_{c,t}} & & \downarrow{\scriptstyle \Pi_{f,t}} \\ \mathbb{R}^N & \xrightarrow{\mathcal{G}_\delta} & \mathcal{C}^2(\Omega,\mathbb{R}^3) \end{array} \tag{14}$$

In other words, we assume that the generated field of a field generator does not depend on its history due to hysteresis effects.

2.2.1. Modeling a Magnetic Field Generator

The regime in which we aim to operate our generator is described in physical terms by the magnetoquasistatic Maxwell's equations (Equation (15) and (16)) and the material equation (Equation (17)).

$$\nabla \times \boldsymbol{H} = \boldsymbol{j}_{\text{app}} \tag{15}$$

$$\nabla \boldsymbol{B} = 0 \tag{16}$$

$$\boldsymbol{B} = \mu_0(\boldsymbol{H}+\boldsymbol{M}) = \mu_0\mu_r\boldsymbol{H} \tag{17}$$

where $\boldsymbol{H}:\mathbb{R}^3\to\mathbb{R}^3$ is the magnetic field strength, $\boldsymbol{j}_{\text{app}}:\mathbb{R}^3\to\mathbb{R}^3$ is the external current density, $\boldsymbol{M}:\mathbb{R}^3\to\mathbb{R}^3$ is the magnetization, and $\boldsymbol{B}:\mathbb{R}^3\to\mathbb{R}^3$ is the magnetic flux density. In particular, the external current density depends directly on the specific configuration δ which describes the spatial arrangement of the conductors and the input currents $\boldsymbol{I}$. The magnetic flux density is source free and directly related to the magnetic field strength $\boldsymbol{H}$ and magnetization $\mathbf{M}$ via Equation (17). Assuming isotropic materials, the magnetic permeability $\mu_r:\mathbb{R}^3\to\mathbb{R}$:

$$\mu_r(\boldsymbol{r}) = \frac{1}{\mu_0}\frac{\partial \mathrm{B}(\boldsymbol{r},|\boldsymbol{H}(\boldsymbol{r})|)}{\partial|\boldsymbol{H}(\boldsymbol{r})|} \tag{18}$$

depends on the material-dependent magnetization curve $\mathrm{B}:\mathbb{R}\to\mathbb{R}$. Since μ_r depends on the magnetization it also inherently contains the geometry of the magnetic material.

Solving this system of partial differential equations for a given configuration $\delta\in\Delta$, input currents $\boldsymbol{I}$, and suitable boundary conditions already provides us with a specific point of the mapping $\mathcal{G}_\delta(\boldsymbol{I}) = \boldsymbol{B}_{\delta,\boldsymbol{I}}$ in Equation (13).

2.3. The Inverse Current Problem

A typical task in the development of new MPI selection field generators $\delta \in \Delta$ is the implementation of measurement sequences. That is, we want to find the input currents $\tilde{\boldsymbol{I}} \in \mathcal{C}^0(\mathbb{T}, \mathbb{R}^N)$ that generate a target magnetic field sequence $\tilde{\boldsymbol{B}} \in \mathcal{C}^2(\Omega \times \mathbb{T}, \mathbb{R}^3)$. This is an inverse problem for which there is generally no analytical solution.

Especially for field generators with many degrees of freedom, i.e., many input currents and corresponding coils, the space of possible solutions can be large. Typically we are interested in low power solutions. Therefore, we formulate the inverse current problem as an optimization problem. Let $\overline{P}_\delta : \mathcal{C}^0(\mathbb{T}, \mathbb{R}^N) \to \mathbb{R}_0^+$ be the time-averaged power consumption of the field generator for input currents $\tilde{\boldsymbol{I}}$. Then, the power-optimal input current sequence $\tilde{\boldsymbol{I}}^*_{\tilde{\boldsymbol{B}}}$ that generates the target magnetic field sequence $\tilde{\boldsymbol{B}}$ is given by

$$\tilde{\boldsymbol{I}}^*_{\tilde{\boldsymbol{B}}} = \underset{\tilde{\mathbf{I}} \in \mathcal{C}^0(\mathbb{R}, \mathbb{R}^N)}{\operatorname{argmin}} \overline{P}_\delta(\tilde{\boldsymbol{I}}) \tag{19}$$

$$\text{s.t. } \tilde{\mathcal{G}}_\delta(\tilde{\boldsymbol{I}}) = \tilde{\boldsymbol{B}} \tag{19a}$$

However, one might run into the problem that there is no solution that generates exactly the desired field sequence. In that case, one has to either change the target field sequence or enlarge the space of potential solutions. We can do the latter, taking into account Section 2.1.5, by optimizing over a larger set of sequences defined by properties such as FFP trajectory or minimum gradient strength. In this case, the inverse current problem is given by

$$\tilde{\boldsymbol{I}}^* = \underset{\tilde{\mathbf{I}} \in \mathcal{C}^0(\mathbb{T}, \mathbb{R}^N)}{\operatorname{argmin}} \overline{P}_\delta(\tilde{\boldsymbol{I}}) \tag{20}$$

$$\text{s.t. } \tilde{\mathcal{G}}_\delta(\tilde{\boldsymbol{I}}) \in \mathcal{B} \tag{20a}$$

where $\mathcal{B}$ is the set of magnetic field sequences with the predefined properties.

As an example, we will illustrate this for our specific use case. For this, we assume that we want to generate an FFP selection field moving along the trajectory $r_{\text{ffp}} : \mathbb{T} \to \Omega$, where we allow spatial deviations within a characteristic range Δx. Furthermore, we want our imaging system not to fall below a certain resolution limit during the multi-patch sequence. Thus, $g > 0$ is introduced as a lower limit for the highest gradient strength and αg, $\alpha \in [0, 0.5]$ as a lower limit for the lowest gradient strength.

If we expand the magnetic field sequence $\tilde{\mathcal{G}}_\delta(\tilde{\boldsymbol{I}}) = \tilde{\boldsymbol{B}}$ for each time $t \in \mathbb{T}$ as in Equation (11) around the position of the target FFP $\boldsymbol{r}_{\text{ffp}}(t)$, we obtain an offset field $\tilde{\boldsymbol{B}}_{\boldsymbol{r}_{\text{ffp}}(t)}(t)$ and a Jacobian matrix $\tilde{\boldsymbol{J}}_{\boldsymbol{r}_{\text{ffp}}(t)}(t)$. The offset field and the eigenvalues $\lambda_1(t)$, $\lambda_2(t)$, and $\lambda_3(t)$ of the latter allow us to mathematically formulate the requirements for our field sequences $\mathcal{B}$. That is, for all $\tilde{\boldsymbol{B}} \in \mathcal{B}$ it should hold that

$$|\lambda_1(t)| \geq g \tag{21}$$

$$|\lambda_3(t)| \geq \alpha g \tag{22}$$

$$\left| \{ \boldsymbol{r} \in \Omega : \tilde{\boldsymbol{B}}(\boldsymbol{r}, t) = 0 \} \right| = 1 \tag{23}$$

$$\frac{\left| \left(\tilde{\boldsymbol{B}}_{\boldsymbol{r}_{\text{ffp}}(t)}(t) \right)_i \right|}{g} \leq \Delta x, i \in \{1, 2, 3\} \tag{24}$$

for all time points $t \in \mathbb{T}$. In detail, Equation (21) and (22) enforce the requirements on the gradient strength, Equation (23) ensures that the FFP field topology does not degenerate by preventing additional FFPs inside the field of view of the MPI system, and Equation (24) keeps the FFP displacement within the bounds set previously.

Note that in the special case of a linear relationship between current and field the total field at the position $\boldsymbol{r}$ can be expressed by a sensitivity matrix $\boldsymbol{S} \in \mathbb{R}^{3 \times N}$ such that $\tilde{\boldsymbol{B}}(\mathbf{r}, t) = \boldsymbol{S}\tilde{I}(t)$. Depending on $\mathcal{B}$, the solution to the optimization problem can then be found by solving a system of linear equations.[53,54] However, in general, the relationship between field and current is nonlinear. A linear relationship can only be assumed for air coils or small currents.

2.4. Design and Optimization of a Field Generator

Finally, we bring together everything we have discussed so far in a novel and general design and optimization approach for magnetic field generators. The central design goal is to find generators that can generate a set of predefined field sequences. These can be, for example, ideal single-patch sequences or general multi-patch sequences which are characterized through the eigenvalues and eigenvectors of the Jacobian matrix. This creates a large design space. The selection of a generator from this space is accomplished by introducing additional optimization goals. For instance, a specific spatial field profile or the average power consumption of the generator may be considered.

The optimization process for a field generator that is to generate a specific set of sequences $\mathfrak{B}$ with minimum average power is shown in **Figure 2**. First, we establish the specific requirements and limitations of the field generator. Consequently, we restrict the design space to a specific subspace $\Delta_{\text{d}} \subset \Delta$. Next, we are searching for the configuration δ of our design space where the arithmetic mean of the power consumption over a given set of measurement sequences $\mathfrak{B}$ is minimal.

$$\underset{\delta \in \Delta_{\text{d}}}{\operatorname{argmin}} \left(\underset{\mathrm{B} \in \mathfrak{B}}{\operatorname{mean}} \left(\min_{\tilde{\mathbf{I}} \in \mathcal{C}^0(\mathbb{T}, \mathbb{R}^N)} \{ \overline{P}_\delta(\tilde{\boldsymbol{I}}) : \tilde{\mathcal{G}}_\delta(\tilde{\boldsymbol{I}}) \in \mathfrak{B} \} \right) \right) \tag{25}$$

It should be noted that this optimization may not result in an optimal outcome. In such a case, it is necessary to redefine the requirements and repeat the aforementioned procedure.

3. Methods

Next, we consider the design and optimization of a specific example of a selection field generator for human-head-sized MPI. We solved the optimization problem as described in Equation (25) to find the most power-efficient generator possible. In this section, we delve into the constraints and prerequisites associated with brain imaging that influence the design space Δ_{d}.

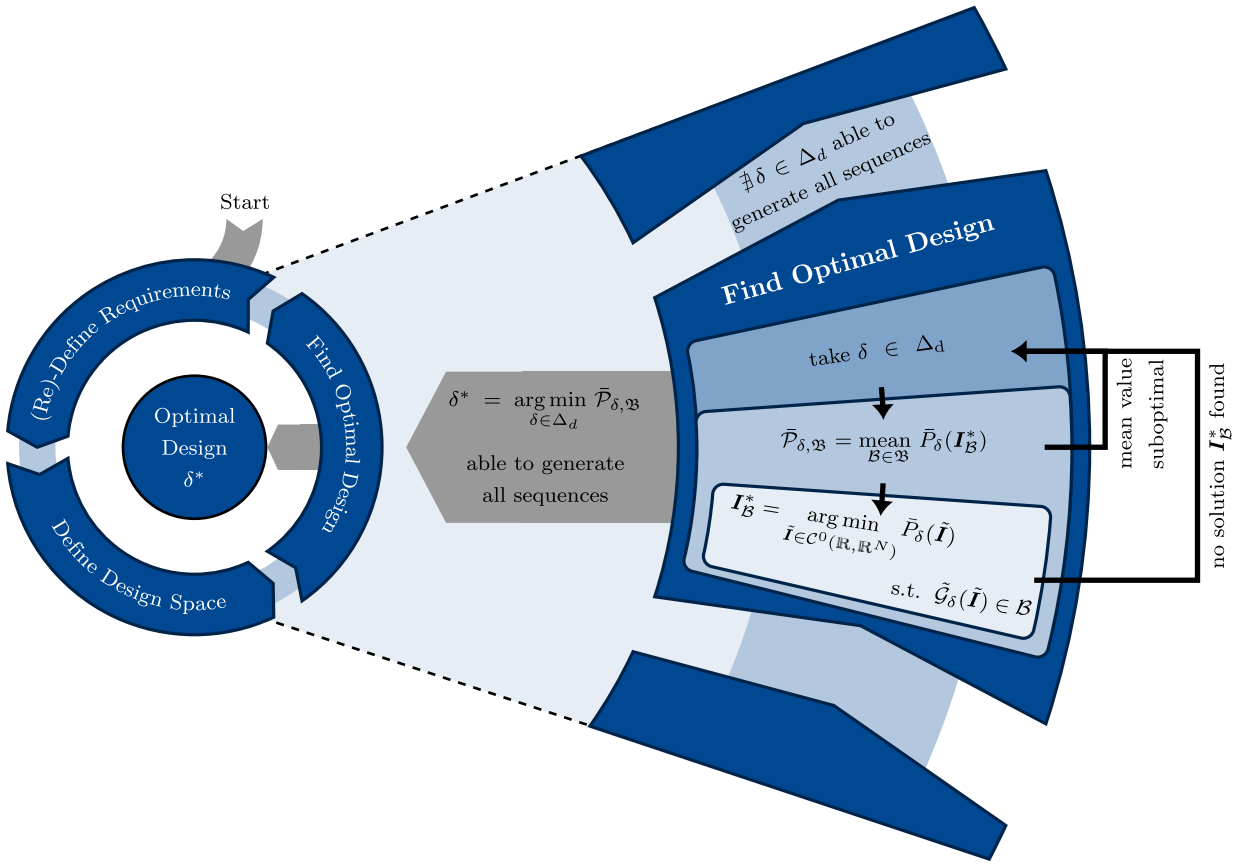

Figure 2. Visualization of the field generator optimization process. The top-level optimization algorithm is shown on the left. It starts with the definition of the field generator requirements, such as the required gradient strength and electrical and mechanical constraints. Based on these requirements, a design space Δ_d is derived. Within the design space Δ_d a geometry optimization process is performed. If an optimal design δ^* is found the optimization process is complete. However, if no optimal design exists within Δ_d the requirements need to be redefined and the process restarts. On the right-hand side a zoom of the geometry optimization process is illustrated which. For a specific design δ, the mean power consumption $\bar{P}_\delta(\boldsymbol{I}^*_{\mathfrak{B}})$ is calculated for a set of field sequences $\mathfrak{B}$ defined in the requirements. To determine the power consumption the corresponding coil currents $\boldsymbol{I}^*_{\mathfrak{B}}$ for the field sequences must be known. The inverse current problem illustrated in the inner box is solved to obtain these currents. The geometry may need to be adjusted if no combination of currents satisfies the constraints and produces the desired field sequences, or if a more efficient solution can be achieved.

3.1. System Requirements

The initial stage in designing magnetic field generators is to define the precise requirements. In the context of an MPI system for human brain imaging, these emerge from both the application itself and the available infrastructure. For our specific case, they can be outlined as follows:

Field Sequences: The imaging system should be able to generate general multi-patch sequences accommodating an FFP. Here, the volume, defined as the FFP generation area, was $18 \times 18 \times 18\,\text{cm}^3 = 5.3\,\text{L}$. For comparison, the typical male human brain has a volume of 1.3 L.[55] The minimum gradient strength $g = 0.22\,\text{Tm}^{-1}$, $\alpha = 0.3$, and $\Delta x = 2\,\text{mm}$ (see Equation (21)–(24)). With this gradient strength, spatial resolutions below 6 mm could be achieved.[56,57] Although better resolutions are possible with higher gradients in this setup for better comparison we limited the gradient strength to that of the current head scanner. To facilitate high-speed imaging, sequences that could provide a complete image of the brain should be able to run at a repetition rate of about 4 Hz.

Power Consumption: The field generator should be able to be operated via a normal household power line. This resulted in an upper limit for the total system power consumption of about 3 kW. Additionally, the system should not be equipped with oil or water cooling. It should only operate with active air cooling, where air is circulated through the system to remove heat from the individual coils. As a result, we limited ourselves to a maximum consumption of 1 kW.

Field Generation: The field generation process should rely solely on electronic FFP movement, avoiding the use of mechanical components. In addition, the system should not contain permanent magnets to allow for complete shutdown of the magnetic fields.

Coil Shape: Coils could exhibit different shapes, such as cylindrical and rectangular configurations. Here, we focused on rectangular coils due to their superior utilization of the construction space. Smaller coils are advantageous for achieving the goal of a high temporal repetition rate for field sequences, as they have a lower inductance and thus higher switching frequencies.

Dimensions: The assembly should be able to accommodate a human head with a movable field-free region to allow imaging of the entire brain. As a result, the coil spacing s was set to 31 cm. A bore width of 19 cm remained when a realistic value of 12 cm was deducted for the copper shielding and the transmitting and receiving coils. According to the work of Zhuang et al. along with the additional space required for the ears, this is suitable for most human heads.[58] The total length of the coil assembly in x and z direction b was limited to 34 cm so that a head could be placed in the center, the excitation coils had enough space, and the patient's shoulders will not be in contact with the field generator (see **Figure 3**).

Structure of Assembly: The assembly should be designed to fit in the copper shielding of our existing MPI system.[56,57,59] Consequently, only coil designs featuring coils on two sides of the patient were considered.

Mass: To comply with building regulations pertaining to ceiling load, the total weight of the field generator should not exceed 400 kg.

Materials: A field generator comprises various materials. Copper was the preferred choice for the coils due to its low electrical resistance and high thermal conductivity. For the iron assembly, different alloys could be utilized. The selection of the alloy affects the power consumption, as variations arise from differences in saturation magnetization and the steepness of the magnetization curve. Laminated materials should be used to maximize switching frequencies and minimize core heating in operation. Here, high-purity soft iron was assumed for the iron parts of the generator. With a saturation magnetization of 2.16 T and low coercivity ≤ 0.2 mT,[60] it provided a good compromise between field-amplification properties and material price.

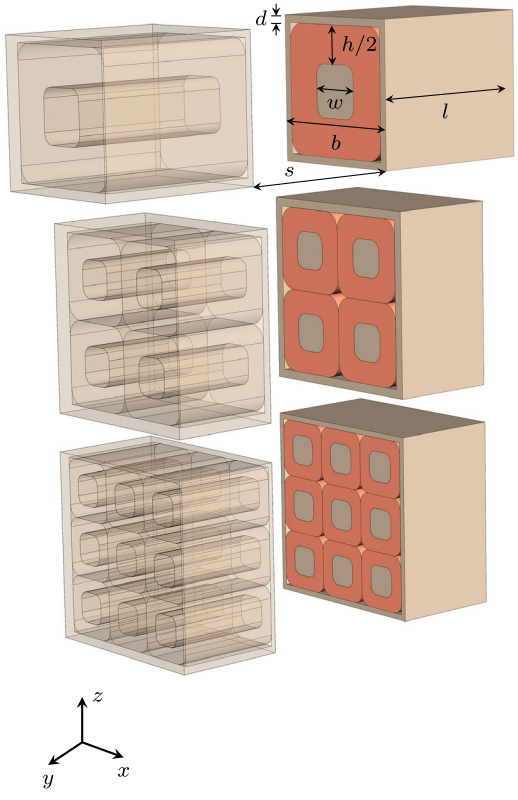

Figure 3. Schematic rendering of the coil setups. The geometry of the optimized field generators with different numbers of coils per side is illustrated. The figure shows the coil lengths l, the core widths w, the coil copper widths h, the iron coating thicknesses d, the coil array spacing s, and the overall coil assembly length in x and z direction b. For the upper design the geometry parameters are $l = 30.5$ cm, $w = 9.9$ cm, $h = 14.3$ cm, $d = 1.4$ cm, $s = 31$ cm, and $b = 27$ cm.

3.2. Design Space

The determination of the design space Δ_d based on the given requirements presents a particularly challenging task and thus needs to be chosen based on prior knowledge and experience in field generator design. On the one hand, computational resources serve as the limiting factor as it is not feasible to optimize over high-dimensional parameter spaces. On the other hand, it is unclear whether configurations exist in the design space that are capable of generating the preset field sequences. Consequently, we were limiting the design space.

Coil Setups: A minimum of 8 coils is required to generate offset and gradient fields.[11] As a result, we considered two setups with 2×2 and 3×3 identical coils per side, which were placed mirror-symmetrically on either side of the field generation volume at a face-to-face distance of $s = 31$ cm as shown in Figure 3. This also ensured manageable construction efforts and signal control. Consequently, the number of coils N was an optimization parameter.

Coil Shape: From the chosen squared geometry, the coil winding thickness h and coil length l appeared as optimization parameters. Note that the rounded corners in Figure 3 only illustrated the finite bending radius of the conductor and were not included in the simulation.

Current Density: The current density ran circular around the central iron core in the xz-plane. Furthermore, it was assumed that the current density in the coils decayed exponentially from the side of each coil facing the patient. The decay constant γ was therefore also an optimization parameter.

Iron Assembly: Prior simulations showed that coils with an inner iron core and outer iron coating as illustrated in Figure 3 guide field lines well into the region between the coils, which helps the generation of the desired fields. As a result, the core thickness of the coils w and the coating thickness d appeared as parameters in the optimization problem.

3.3. Design Optimization

The simulation of individual designs is computationally demanding, necessitating a further reduction of the design spaces' dimensionality. For this purpose, a simplified setup with two coils and 1D FFP motion was considered first. The 3D design space was small enough to find an optimal coil geometry. Initial simulations with an upper bound on the mass consistently yielded designs with maximum mass. To further reduce the design space this and subsequent studies used the mass as a constraint, allowing the coil length l to be eliminated as an independent parameter from the grid search. Consequently, for the

simulation l was always scaled to reach the maximum mass. The optimization parameters considered in this study were the coil winding thickness h, core width w, outer iron layer width d, and the current density decay constant γ (see Figure 3 and Appendix A). A grid search was performed with five points per interval, defining the basic geometry of the entire setup. As field sequences, we considered a uniform movement of the FFP along the y axis between $r_y = \pm 45$ mm where $r_y = 0$ represents the face-centered midpoint on the axis. The optimal current sequence that generated this field sequence could be found using Equation (19) in conjunction with Equation (21)–(24). The mean power consumption for this sequence was approximated by quadrature for each geometry parameter combination; i.e. by summing the power of starting, center, and end point of the sequence, which correspond to FFP positions $r_y = 0$mm and $r_y = \pm 45$mm.

The findings from this pre-optimization could be used to define a suitable design space Δ_d for the 3D MPI scanners in a second step. Two designs with 2×2 and 3×3 coils per side were optimized separately in terms of their geometry by performing a grid search. We used a central static FFP as the field sequence and the required power was determined analogously to previous optimization by solving the inverse current problem. The fact that we have limited ourselves to a single FFP position here was also due to the high computational effort. An additional parameter could be eliminated from the grid search by setting the total length of the coil assembly in x and z direction b to its maximum of 34 cm. This was a valid choice as it was known from the previous study that the coil side length played the most important role in the effectiveness of the setup. The remaining optimization parameters were the width of the core w, the outer iron layer width d, and the current density decay constant γ.

In a third step the geometric optima for both cases were used to calculate the power consumption of the system for a spatial grid of FFP positions that were representative for any continuous FFP field sequence in a volume of $18 \times 18 \times 18\,\text{cm}^3$. Specifically, $\mathfrak{B}$ was set to 343 static field sequences with FFP positions on a centered $7 \times 7 \times 7$ grid, with a grid spacing of 3 cm. This setup could be used to determine the optimum number of coils per side for our application.

In this study, the commercial software COMSOL (COMSOL Multiphysics v.6.0. www.comsol.com. COMSOL AB, Stockholm, Sweden, COMSOL Multiphysics) was used to numerically approximate the mapping $\boldsymbol{B}_{\delta,I}$. Material properties such as the magnetization curve of the materials were extracted from the COMSOL material library. Additionally, the LiveLink for MATLAB (MATLAB 9.14.0 (R2023a), https://www.mathworks.com, The MathWorks Inc. Natick, Massachusetts) was used to automate the calculations. Further details on the field calculation and solution of the inverse problem as well as the exact ranges of the optimization parameters can be found in Appendices A–C.

4. Results

In the following the optimization results for the pre-optimization and the geometry optimization of the 3D MPI field generators are presented.

4.1. Single Coil per Side

The optimization result demonstrates the potential power savings achievable by adhering to the current field production concept of using two coils. The system's average power consumption is determined to be 17 W for symmetrical FFP movement along the y axis spanning 9 cm between the coils. For comparison, the average power for a similar FFP movement with our current head scanner selection field assembly is about 400 W.[56,57] In the explored design space, the optimum values for the optimization parameters are $l = 30.5$ cm, $w = 9.9$ cm, $h = 14.3$ cm, $d = 1.4$ cm and $\gamma = 1.0\,\text{m}^{-1}$.

In **Figure 4**, the sensitivity to the optimization parameters is shown. In Figure 4a–e it is clearly visible that in this regime the coils copper width h and its iron core width w play the most important role for the power consumption of the setup. The dependence on the parameter γ is rather weak compared to h and w (see Figure 4d,e). Its optimum value $\gamma = 1\ \text{m}^{-1}$ corresponds to a nonuniform current distribution along the coil. The dependence on the coating thickness d is rather complex. Depending on the intersection of the optimization parameters, a change in d seems to have different effects on the power consumption (see Figure 4b,c,f). For some combinations of h and w, a smaller d is better, for others a larger one.

4.2. Geometry Optimization of 3D MPI Field Generator

The results for the geometry parameter grid search for the setup with 2×2 and 3×3 coils per side are summarized in **Figure 5**. It shows the power consumption of the system for a central FFP with a gradient strength of $0.22\,\text{Tm}^{-1}$ as a function of various geometry parameters. Slices through the parameter space are visible, each containing the optimum.

The optimal configuration for the 2×2 setup leads to a power consumption of 240 W for a central FFP. This is the case for $l = 18.7$ cm, $\gamma = 4.9\,\text{m}^{-1}$, $d = 1.6$ cm, and $w = 7.0$ cm. Here the power consumption is most sensitive to the iron core width w (see Figure 5(2b),(2c)). Smaller γ and larger d are also advantageous but do not affect the power quite as much as w (see Figure 5(2a)–(2c)). It is likely that the global minimum is not in the design space since the optimum is located at the edge of the parameter space for all parameters.

The optimal configuration for the 3×3 setup offers a power consumption of 200 W for a central FFP with the same gradient strength. The corresponding parameters are $l = 19.3$ cm, $\gamma = 4.9\,\text{m}^{-1}$, $d = 1.0$ cm, and $w = 5.6$ cm. Once again, the power consumption is most sensitive to the width of the iron core w (see Figure 5(3b),(3c)). γ and d also visibly affect the power consumption, but γ has the weakest influence (see Figure 5(3a)–(3c)). While the optimum for w and d lies within the parameter interval under consideration, the optimum for γ lies on the edge. Note that in Figure 3 the field generators are plotted with their optimal geometry parameters in the design space.

4.3. Comparison of Optimized Generators

Using the optimal parameters, the power consumption of both systems for $7 \times 7 \times 7$ single-patch sequences is shown in

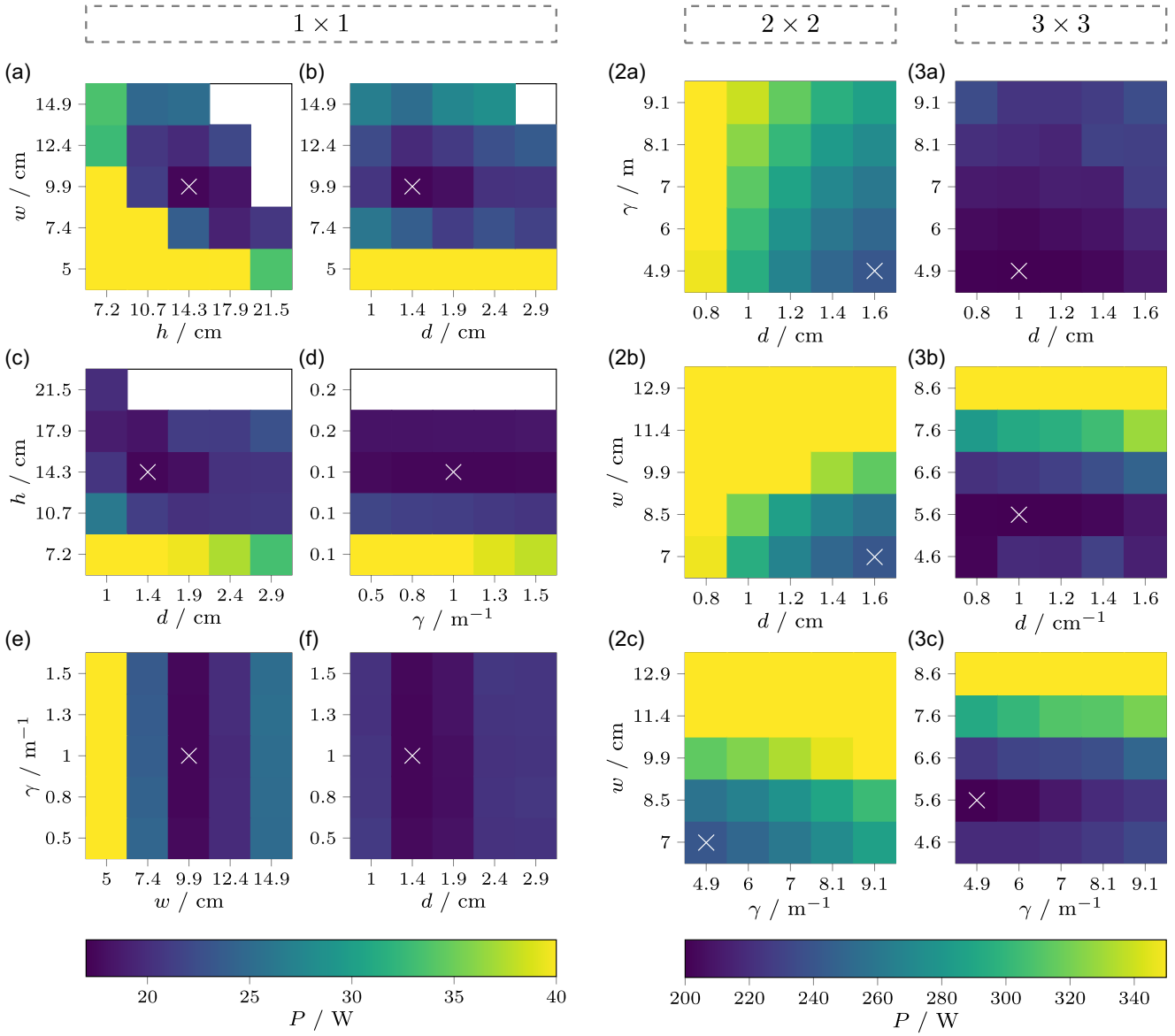

Figure 4. Mean power consumption for 1D FFP movement with two coils and different geometry parameters. a–f show cross sections through the design space depending on w, h, d and γ. The gradient strength is set to $g = 0.22\,\mathrm{T\,m^{-1}}$ while the unvaried parameters are held at their optimum. The power optimum of 17 W is marked by a white cross. In each case regions of the design space that do not comply with the mass constraints have been omitted. The power plots provide an estimate of how sensitive the field generator reacts to changes in certain geometry parameters with regard to its power consumption. The thickness of the copper cross section and the iron core play the biggest role. The power is less dependent on the thickness of the iron coating and the drop in current density. The spatial profile around the optimum is an indicator that there is no other local optimum in the vicinity.

Figure 5. Geometry optimization results of a 3D MPI field generator. Every plot shows the power consumption of a 3D MPI field generator for a central FFP with a gradient strength of $0.22\,\mathrm{T\,m^{-1}}$ for different parameters. On the left, different geometry parameters are varied for a setup with a 2×2 coil array on every side (2a–2c) and on the right different geometry parameters are varied for a 3×3 coil array (3a–3c). The geometry parameters are the current density decay parameter γ, the iron core width w and the iron coating thickness d (see Figure 3). The white cross indicates the location of the optimum inside the design space. It is ≈240 W for the 2×2 setup and ≈200 W for the 3×3 setup. In the 3×3 design, the optimum is well within the design space for all parameters except γ. For the 2×2 design, in contrast, the optimum for all parameters is at the edge of the design space. This is indicates that there are designs outside the design space with even lower power consumption for a central FFP.

Figure 6. High power consumption above 400 W occurs more frequently for the 2×2 design for FFP positions near the coils, especially for $z = 0\,\mathrm{cm}$. In comparison, they are observed less frequently for the 3×3 design. These positions tend to be at the edge of the field generation volume with a large accumulation at $z = 9\,\mathrm{cm}$. Low power consumption of less than 100 W can be observed in close proximity of the coils for the 3×3 design only.

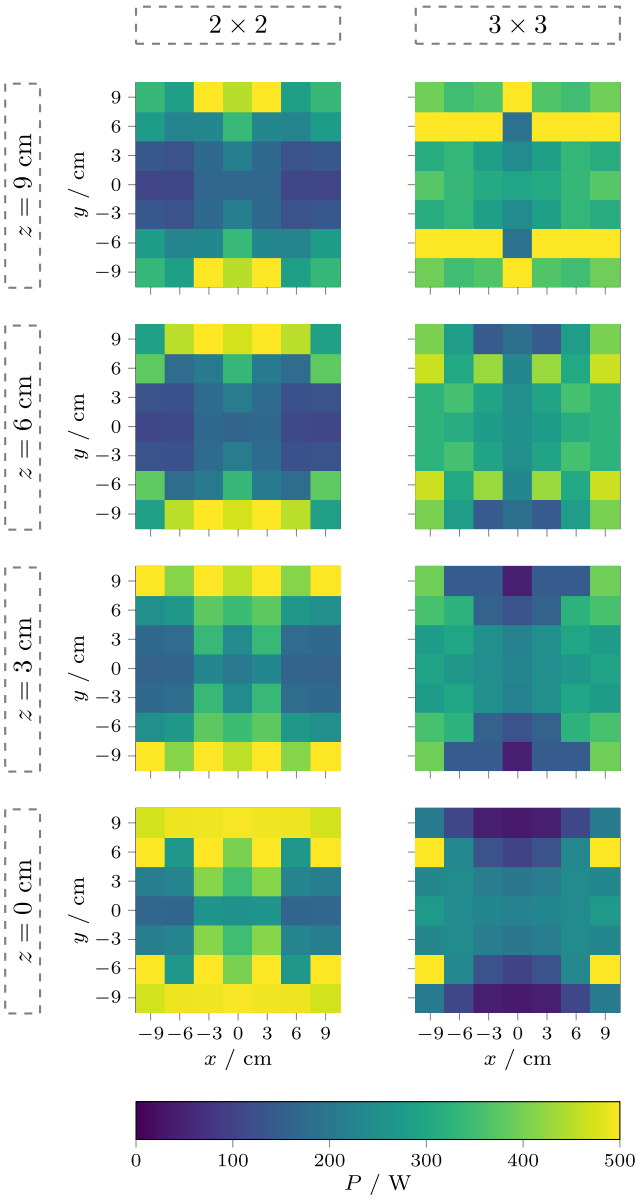

Figure 6. Results for 3D FFP displacement with different number of coils per coil housing. Here, static field sequences $\mathcal{B}$ in which the FFP is generated at a certain point in 3D grid with a gradient of $g = 0.22\,\mathrm{Tm}^{-1}$ are considered. The left side shows the results for the design 2×2 coils and the right side with 3×3 coils. In each case, the xy plane for different z values can be seen. It is visible that the coil design with 8 coils requires very high power for FFP generation, especially at the edges. The design with 18 coils can achieve significantly lower power values in these regions by properly selecting the currents.

The distribution of the power consumption for $7 \times 7 \times 7$ single-patch sequences is shown in **Figure 7**. The histogram confirms the observations regarding the frequency of low and high power consumption. Visually, neither of the two distributions is superior to the other in terms of average power consumption. The mean power consumption is $(330 \pm 220)\,\mathrm{W}$ and $(310 \pm 150)\,\mathrm{W}$ for the 2×2 and 3×3 designs, respectively.

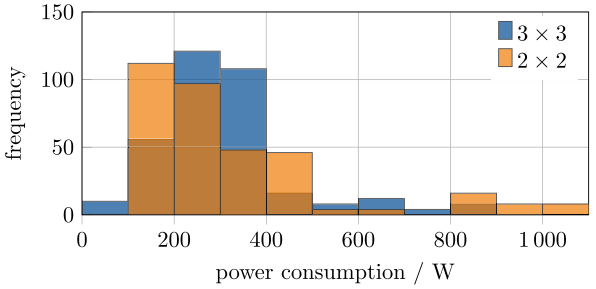

Figure 7. Histogram of power consumption for both field generators creating FFPs. A total 343 field sequences with FFPs located on a grid are considered. The grid spans a volume of $18 \times 18 \times 18\,\mathrm{cm}^3$ and has a grid spacing of 3 cm.

While the mean power consumption for both designs is quite similar, their maxima are 1040 W and 820 W for the 2×2 and 3×3 designs, respectively.

5. Discussion

Magnetic field generators are integral to most imaging systems. This study focuses on the design and optimization of selection field generators, which are responsible for generating the slow slew fields essential for large field of view systems. The design of a field generator is primarily dictated by the field sequences to be generated. According to standard system specifications numerous designs are capable of accomplishing these necessities. We developed and formalized an approach for designing and optimizing, focused on searching for the lowest average power consumption design within this space. We then used this optimization process to design a magnetic field generator specifically for a human MPI brain imaging system.[56,57]

The design process of a magnetic field generator is an optimization problem. Key parts of the formulation are a mathematical model of magnetic field generators, a mathematical formalism to define field sequences, and a relationship between power consumption and field sequence. The latter is an inverse problem referred to as the inverse current problem. For field generators operating with soft magnetic materials outside the linear regime the inverse current problem also becomes nonlinear.

With respect to imaging field sequences, we have defined a set hierarchy of multi-patch sequences on the basis of the properties of the local fields. Axis-aligned gradient fields that are gradually shifted are the standard cognitive model for FFP multi-patch sequences. These sequences define the set of focus-field-based multi-patch sequences at the bottom of the hierarchy. Similarly, dynamic FFL multi-patch sequences utilize axis-aligned gradient fields that are simultaneously rotated and shifted. These sequences belong to the set of dynamic gradient-based multi-patch sequences one level up in the hierarchy. We have also defined a more universal set, the general multi-patch sequence, which includes the aforementioned sequences but does not restrict the gradient field to ideal ones. This generalization has two advantages. First, it better describes existing MPI systems where ideal fields occur in a small volume at the scanner center only. Secondly, it offers a much larger space for the design

of multi-patch sequences, for example by limiting the minimum gradient of the sequence to the smallest eigenvalue of the Jacobian matrix. In this work, we designed a power-optimized MPI field generator that exploits these less stringent requirements on the fields to be generated.

Due to the size of the design space the optimization process for the selection field generator for MPI brain imaging is a multistage process. It is divided into a pre-optimization with a generator restricted to 1D FFP movements and a subsequent optimization which considers generators that allow for 3D FFP movements. In the pre-optimization a simplified 1×1 coil structure is geometrically optimized. The parameters from this study are downscaled to the smaller coils of the 2×2 and 3×3 setup. These serve as reference points to define the design space of the generators for the 3D FFP motion. The geometry optimization for 3D FFP movement itself is also a two-stage process. First, the geometry parameters for a setup with 2×2 and a setup with 3×3 coils are optimized independently of each other for a field sequence with a central static FFP. Next, the setups are compared with each other by extending the field sequence to a grid of FFP positions.

In our work, optimization takes place via grid searches. This allows studying the influence of the field generator's different design parameters on the average power consumption. In the pre-optimization, a local minimum for the optimal design parameters for the presented 1×1 design was found. The system's power requirement is primarily influenced by the thickness of the core, denoted by w, and the cross-sectional area of the copper component, represented by h. While the thickness of the iron coating d reduces the power needed for the coil, the impact is not as significant as the other parameters in the selected design space. These observations corroborate those made during the optimization of the 2×2 and 3×3 designs. Additionally, the pre-optimization results indicate that maximizing the side length of the entire structure is crucial. Note that the downscaled ratio of core size to copper cross section from the pre-optimization is far from the optimum value of the 3D FFP generators, which are located at the edge of the design space. Therefore, the considered part of the design space probably contained only suboptimal ratios. The results of the pre-optimization show that a nonuniform current density distribution along the coil axis is optimal. Since the optimum value for the current density decay parameter γ is at the edge of the design space for the 3D FFP generators, we cannot draw the same conclusion in this case. However, we find it unlikely that a uniform current distribution is optimal.[15]

With an average power of 17 W for a field sequence with a linear 9 cm FFP movement at a gradient strength of $0.22\,\mathrm{Tm}^{-1}$, the 1×1 field generator is 20 times more efficient than the current head scanner.[56,57] For the 3D FFP generators the power consumption was determined at the same gradient strength for a set of $7 \times 7 \times 7$ single-patch sequences in the FFP generation area. Assuming that hysteresis effects within the soft magnetic material of the field generator are negligible, the power consumption of the set of single-patch sequences is a good estimate of the power consumption of dynamic multi-patch sequences. With (330 ± 220) W for the 2×2 and (310 ± 150) W for the 3×3 generator the average power for both generator candidates are comparatively similar. The 2×2 design has the larger standard variation, larger maximum power consumption, and also slightly violates the previously defined upper limit of 1 kW. Comparing the generators for a 1D and central FFP movement in y direction with a length of 12 cm with the magnetic field generator of the current head scanner, the average power is reduced by about 50% for the 2×2 design and by about 75% for the 3×3 design. During operation of such a generator the heat produced must be dissipated. Depending on the cooling concept this is only possible up to a certain power limit. As a guiding value, we consider the maximum power dissipation during a 1D FFP sequence of our current head scanner to be around 440 W. 78% for the 2×2 and 88% for the 3×3 generator of the single-patch sequences considered are each below this power value indicating that the 3×3 design is easier to cool. Spatially, the sequences with high power consumption for the 2×2 generator accumulate in front of the coils and in the central z slice ($z = 0$ cm). For the 3×3 generator, there is an accumulation of high power values at the bottom and top of the FFP generation area ($z = \pm 9$ cm). The frequency and localization of high power consumption single-patch sequences indicate that it is easier to dissipate the generated heat for the 3×3 design in continuous operation.

6. Outlook

In the entire design space of all field generators we could only optimize within a small subspace due to limited computational resources. Thus, it is likely that much more efficient field generator designs exist. One promising approach is to place the coils closer to the field generation region by placing them at an angle around the patient's head.[32]

In terms of power consumption the 3×3 field generator was optimal. From a manufacturing and operational perspective, the 3×3 design presents challenges compared to the 1×1 and 2×2 design that we did not yet addressed in this work. However, the individual coils of the 3×3 design have significantly smaller inductances. As a result, only little reactive power is required to change the current in the coils, which increases the switching frequencies and makes it easier to turn off the coils quickly. As the size of the generator increases the magnetic forces on the built-in components play an increasingly important role. This must then also be considered in the mechanical design of the generator.[15]

The presented design optimization method is aimed at reducing power consumption. However, because it is highly adaptable it has broader applications . For example, also field generation by permanent magnets could be taken into account. Alternative optimization goals, including the generation of maximum gradients from a field generator under identical system requirements, are feasible by modifying the optimization problem to specifically affect other generator characteristics.

7. Conclusion

This study presents a methodology for designing and optimizing magnetic field generators using soft magnetic materials operating in the nonlinear regime. The presented method can produce

magnetic field generators that have high field strengths and gradients, large field generating volumes, and minimal power consumption. Using this methodology we have developed a first MPI selection field generator designed from scratch with soft magnetic materials operating in the nonlinear regime, which significantly increases the FFP generation volume of our current brain imaging system while decreasing the average power consumption. The main objective during optimization was to minimize the power consumption of the field generator as it poses a significant barrier to the scaling of MPI systems. Generally, the method outlined can be extended beyond the MPI context to other areas that employ magnetic field generators with similar capabilities and scaling obstacles, such as the magnetic manipulation of medical devices and microrobots.

Appendix

A Simulation Details

To solve the forward problem from currents to magnetic field, Maxwell's equations (Equation (15) and (16)) are usually converted to an equivalent system of equations, which can be derived by introducing the magnetic vector potential $\boldsymbol{A}$

$$\boldsymbol{B} = \nabla \times \boldsymbol{A}. \tag{26}$$

Using the Coulomb gauge ($\nabla \boldsymbol{A} = 0$), Equation (16) is always satisfied and Equation (15) and (17) can be equivalently formulated as

$$\nabla^2 \boldsymbol{A} = -\mu_0 \mu_r \boldsymbol{j}_{\text{app}}. \tag{27}$$

Here, $\mathbf{j}_{\text{app}}$ is the applied current density, which can be expressed as $\boldsymbol{j}_{\text{app}} = \sum_{i=1}^{N} \boldsymbol{j}_i$ where $\boldsymbol{j}_i : \mathbb{R}^3 \to \mathbb{R}^3$ are the individual coil current densities of the generator. Note that μ_r depends on $\boldsymbol{A}$ due to Equation (18) and (26). It is assumed that the current density of the ith coil decays exponentially as

$$\boldsymbol{j}_i(\boldsymbol{r}) = \begin{cases} \boldsymbol{j}_{i,0}(r_x, r_z) e^{-\gamma(\frac{1}{2}s - |r_y|)} & \boldsymbol{r} \in V_i \\ 0 & \text{else} \end{cases} \tag{28}$$

from the coil face on the patient side to its end with the decay constant γ. Here, $\boldsymbol{j}_{i,0} : \mathbb{R}^2 \to \mathbb{R}^3$ indicates the direction of the current density and $V_i \subset \mathbb{R}^3$ indicates the volume of the ith coil. Additionally, we assume a constant absolute value of the current density in one slice of the xz-plane such that $|\boldsymbol{j}_{i,0}(r_x, r_z)| = j_{i,0}, \forall \boldsymbol{r} \in V_i$. s is the distance between both coil cages (see Figure 3).

Such a system of semi-linear partial differential equations is commonly solved using finite-element methods (FEMs).[61] To calculate the power P_i of each multi-turn coil it is assumed that the coils are wound from a single wire with a cross-sectional area of $q = 1\,\text{mm}^2$ made of copper with a fill factor of 1. Subsequently, the length L of this wire is approximated as

$$L = \frac{lh}{q}(2w + h) \tag{29}$$

and consequently the power

$$P_i = \frac{L \rho_{\text{cu}} q^3 j_{i,0}^2}{2\gamma l}\left(1 - e^{-2\gamma l}\right) \tag{30}$$

is determined using the specific resistance of copper ρ_{cu}.

The FFP position and the Jacobian matrix at the expansion point can be determined using various methods. In a real-world scenario a Hall probe can be employed to measure the magnetic field and the field can be evaluated on a grid, which is the most straightforward option.

In this work field values and field derivatives are computed using the field measurement method introduced by Boberg et al.[62] A spherical 10-design with a radius of 2 cm and 62 measuring points is integrated in the FEM mesh and utilized for 3D FFP movement. The spherical 10-design is centered around the target FFP position, respectively. For the 1D FFP movement with two coils, a spherical 2-design with a radius of 1 cm and two measuring points is used.

B Algorithms and Calculation Strategy

There are different optimization algorithms to solve the inverse current problem. In a regime with a linear relationship between coil currents and the generated field, it reduces to inverting a matrix.[54] When nonlinear effects play a role the problem must be solved iteratively. Here, the method of moving asymptotes[63] is used as the optimization algorithm, which is implemented in COMSOL.A suitable set of starting currents has to be found for the optimization. The first step is to calculate the currents for an FFP at a symmetry point of the setup. The fact that the currents at this point also satisfy certain symmetry conditions makes it easier to find suitable initial values. Once an efficient set of currents has been determined they can be used as new starting currents for a nearby FFP or a similar field constellation in general, which reduces the number of iterations required during optimization.

The symmetry properties of the systems can also be exploited to keep simulation times low. For example, to infer the power consumption of the 1D FFP generator, the power consumption of two static FFP field sequences has to be calculated. The remaining power value is obtained by mirroring. In the case of the 3D field generators for the field sequences forming a $7 \times 7 \times 7$ FFP grid, only $4 \times 4 \times 4$ power values for FFP positions in one octant of the volume need to be calculated. The remaining values can also be obtained by mirroring.

C Methods Details

In the simplified setup two coils are positioned facing each other, resembling the current field generator design of the head scanner. The coil-shape parameters are optimized with respect to an axial FFP movement. The optimization parameters are summarized in **Table 1**. Five discrete values are selected in an interval and a grid search is performed for all combinations of parameters.

For the geometry optimization of the 3D FFP movement field generator, a 2×2 and 3×3 matrices are considered. In addition to the length of the coil l, a further parameter can be eliminated from the optimization by setting the total length of the assembly b to its maximum of 34 cm. The two linear equations 34 cm =

Table 1. Optimization parameter ranges for two coils facing each other.

Geometry Parameters	1×1
Coils winding thickness h	$\in [7.2\ \text{cm},\ 21.5\ \text{cm}]$
Core width w	$\in [5.0\ \text{cm},\ 14.9\ \text{cm}]$
Outer iron coating width d	$\in [1.0\ \text{cm},\ 2.9\ \text{cm}]$
Current density decay constant γ	$\in [0.5\ \text{m}^{-1}, 1.5\ \text{m}^{-1}]$

Table 2. Optimization parameter ranges for 3D FFP movement.

Geometry Parameters	2×2	3×3
Core width w	$\in [7.0\ \text{cm},\ 12.9\ \text{cm}]$	$\in [4.6\ \text{cm},\ 8.6\ \text{cm}]$
Outer iron coating width d	$\in [0.8\ \text{cm},\ 1.6\ \text{cm}]$	$\in [0.8\ \text{cm},\ 1.6\ \text{cm}]$
Current density decay constant γ	$\in [4.9\ \text{m}^{-1}, 9.1\ \text{m}^{-1}]$	$\in [4.9\ \text{m}^{-1}, 9.1\ \text{m}^{-1}]$

$2(d + h + w)$ and $34\,\text{cm} = 2d + 3(h + w)$ can be used for the 2×2 and 3×3 configurations, respectively. The optimization parameters are listed in **Table 2**. Again, for each of the optimization parameters, five discrete values are selected in an interval and a grid search is performed for all combinations of parameters.

Acknowledgements

Publishing fees are supported by Funding Programme Open Access Publishing of Hamburg University of Technology (TUHH).

Open Access funding enabled and organized by Projekt DEAL.

Conflict of Interest

The authors declare no conflict of interest.

Data Availability Statement

The data that support the findings of this study are available from the corresponding author upon reasonable request.

Keywords

biomedical imaging, geometry optimization, magnetic actuation, magnetic field generator, magnetic particle imaging, nonlinear inverse problems, soft iron

Received: January 5, 2024
Revised: June 21, 2024
Published online: August 22, 2024

[1] W. E. Brant, C. A. Helms, *Fundamentals of Diagnostic Radiology*, Lippincott Williams & Wilkins, Philadelphia **2012**.
[2] Z. Liang, P. C. Lauterbur, *IEEE Signal Process. Mag.* **2002**, *19*, 86.
[3] V. P. B. Grover, J. M. Tognarelli, M. M. E. Crossey, I. J. Cox, S. D. Taylor-Robinson, M. J. W. McPhail, *J. Clin. Experim. Hepatol.* **2015**, *5*, 246.
[4] T. Knopp, N. Gdaniec, M. Möddel, *Phys. Med. Biol.* **2017**, *62*, R124.
[5] A. Mukhatov, T. Le, T. T. Pham, T. D. Do, *Nano Select.* **2023**, *4*, 213.
[6] Z. Yang, L. Zhang, *Adv. Intell. Syst.* **2020**, *2*, 2000082.
[7] B. J. Nelson, I. K. Kaliakatsos, J. J. Abbott, *Annu. Rev. Biomed. Eng.* **2010**, *12*, 55.
[8] Y. Hou, H. Wang, R. Fu, X. Wang, J. Yu, S. Zhang, Q. Huang, Y. Sun, T. Fukuda, *Lab Chip* **2023**, *23*, 848.
[9] C. Limpabandhu, Y. Hu, H. Ren, W. Song, Z. T. Ho Tse, *Proc. Inst. Mech. Eng., Part H* **2023**, *237*, 297.
[10] J. Rahmer, D. Wirtz, C. Bontus, J. Borgert, B. Gleich, *IEEE Trans. Med. Imaging* **2017**, *36*, 1449.
[11] R. Chen, D. Folio, *Curr. Robot. Rep.* **2022**, *3*, 119.
[12] B. Gleich, J. Weizenecker, *Nature* **2005**, *435*, 1214.
[13] A. C. Bakenecker, J. Schumacher, P. Blümler, K. Gräfe, M. Ahlborg, T. M. Buzug, *Phys. Med. Biol.* **2020**, *65*, 195014.
[14] K. Sajjamark, J. Franke, H. Lehr, R. Pietig, V. Niemann, *Int. J. Magn. Part. Imaging* **2021**, *7*, 2201001.
[15] C. Bontus, B. Gleich, B. David, O. Mende, J. Borgert, *IEEE Trans. Magn.* **2015**, *51*, 1.
[16] T.-A. Le, M. P. Bui, J. Yoon, *IEEE/ASME Trans. Mechatron.* **2021**, *26*, 551.
[17] X. Zhang, T.-A. Le, A. K. Hoshiar, J. Yoon, *IEEE/ASME Trans. Mechatron.* **2018**, *23*, 1573.
[18] J. Rahmer, B. Gleich, C. Bontus, I. Schmale, J. Schmidt, J. Kanzenbach, O. Woywode, J. Weizenecker, J. Borgert, *ISMRM Abstract* **2011**, 1.
[19] J. Rahmer, B. Gleich, J. Weizenecker, A. Halkola, C. Bontus, J. Schmidt, I. Schmale, O. Woywode, T. Buzug, J. Borgert, in *2013 International Workshop on Magnetic Particle Imaging (IWMPI)*, IEEE, Piscataway, NJ **2013**, pp. 1–1.
[20] J. Weizenecker, C. Bontus, J. Rahmer, J. Schmidt, J. Kanzenbach, J. Borgert, in *Proc. Intl. Soc. Mag. Reson. Med. 18*. Stockholm, **2010**.
[21] J. Rahmer, C. Stehning, B. Gleich, *PLoS One* **2018**, *13*, e0193546.
[22] J. J. Konkle, P. W. Goodwill, D. W. Hensley, R. D. Orendorff, M. Lustig, S. M. Conolly, *PLoS One* **2015**, *10*, e0140137.
[23] P. W. Goodwill, J. J. Konkle, B. Zheng, E. U. Saritas, S. M. Conolly, *IEEE Trans. Med. Imaging* **2012**, *31*, 1076.
[24] K. Bente, M. Weber, M. Graeser, T. F. Sattel, M. Erbe, T. M. Buzug, *IEEE Trans. Med. Imaging* **2015**, *34*, 644.
[25] A. Tonyushkin, *IEEE Trans. Magn.* **2017**, *53*, 1.
[26] P. Vogel, M. A. Rückert, P. Klauer, W. H. Kullmann, P. M. Jakob, V. C. Behr, *IEEE Trans. Med. Imaging* **2014**, *33*, 400.
[27] P. Vogel, M. A. Rückert, C. Greiner, J. Günther, T. Reichl, T. Kampf, T. A. Bley, V. C. Behr, S. Herz, *Sci. Rep.* **2023**, *13*, 10472.
[28] A. W. Mahoney, J. C. Sarrazin, E. Bamberg, J. J. Abbott, *Adv. Robot.* **2011**, *25*, 1007.
[29] T. Xu, G. Hwang, N. Andreff, S. Regnier, *IEEE Trans. Robot.* **2015**, *31*, 117.
[30] K. B. Yesin, K. Vollmers, B. J. Nelson, *Int. J. Robot. Res.* **2006**, *25*, 527.
[31] S. Jeong, H. Choi, J. Choi, C. Yu, J.-O. Park, S. Park, *Sens. Actuators, A* **2010**, *157*, 118.
[32] M. P. Kummer, J. J. Abbott, B. E. Kratochvil, R. Borer, A. Sengul, B. J. Nelson, *IEEE Trans. Robot.* **2010**, *26*, 1006.
[33] D. Son, X. Dong, M. Sitti, *IEEE Trans. Robot.* **2019**, *35*, 343.
[34] S. Salmanipour, E. Diller, in *2018 IEEE International Conference on Robotics and Automation (ICRA)*, IEEE, Brisbane, QLD, **2018**, pp. 3608–3613, ISBN: 978-1-5386-3081-5, https://ieeexplore.ieee.org/document/8461026/.
[35] F. Griese, T. Knopp, C. Gruettner, F. Thieben, K. Müller, S. Loges, P. Ludewig, N. Gdaniec, *J. Magn. Magn. Mater.* **2020**, *498*, 166206.
[36] A. C. Bakenecker, A. von Gladiss, T. Friedrich, U. Heinen, H. Lehr, K. Lüdtke-Buzug, T. M. Buzug, *J. Magn. Magn. Mater.* **2019**, *473*, 495.
[37] T. Knopp, T. M. Buzug, *Magnetic Particle Imaging*, Springer Berlin Heidelberg, Berlin, Heidelberg **2012**.

[38] T. Kluth, *Inverse Probl.* **2018**, *34*, 083001.
[39] J. Rahmer, J. Weizenecker, B. Gleich, J. Borgert, *BMC Med. Imaging* **2009**, *9*, 4.
[40] O. Dössel, J. Bohnert, *Biomedizinische Technik/Biomed. Eng.* **2013**, *58*, 611.
[41] J. Bohnert, Ph.D. Thesis, *Karlsruhe Institute of Technology*, Karlsruhe **2012**, https://www.ksp.kit.edu/site/books/m/10.5445/KSP/1000025255/.
[42] E. U. Saritas, P. W. Goodwill, G. Z. Zhang, S. M. Conolly, *IEEE Trans. Med. Imaging* **2013**, *32*, 1600.
[43] J. Weizenecker, B. Gleich, J. Rahmer, H. Dahnke, J. Borgert, *Phys. Med. Biol.* **2009**, *54*, L1.
[44] B. Gleich, J. Weizenecker, H. Timminger, C. Bontus, I. Schmale, J. Rahmer, J. Schmidt, J. Kanzenbach, J. Borgert, *Proc. ISMRM* **2010**, *18*, 1920.
[45] P. W. Goodwill, S. M. Conolly, *IEEE Trans. Med. Imaging* **2011**, *30*, 1581.
[46] C. Kaethner, M. Ahlborg, G. Bringout, M. Weber, T. M. Buzug, *IEEE Trans. Med. Imaging* **2014**, *34*, 381.
[47] T. Knopp, K. Them, M. Kaul, N. Gdaniec, *Phys. Med. Biol.* **2015**, *60*, L15.
[48] P. Szwargulski, M. Möddel, N. Gdaniec, T. Knopp, *IEEE Trans. Med. Imaging* **2018**, *38*, 932.
[49] P. W. Goodwill, S. M. Conolly, *IEEE Trans. Med. Imaging* **2010**, *29*, 1851.
[50] N. Gdaniec, P. Szwargulski, T. Knopp, *Med. Phys.* **2017**, *44*, 6456.
[51] J. J. Konkle, P. W. Goodwill, O. M. Carrasco-Zevallos, S. M. Conolly, *IEEE Trans. Med. Imaging* **2013**, *32*, 338.
[52] M. Boberg, T. Knopp, P. Szwargulski, M. Möddel, *IEEE Trans. Med. Imaging* **2019**, *39*, 1347.
[53] C. Kaethner, M. Ahlborg, T. Knopp, T. F. Sattel, T. M. Buzug, *J. Appl. Phys.* **2014**, *115*, 044910.
[54] F. Foerger, M. Graeser, T. Knopp, *Int. J. Magn. Part. Imaging* **2020**, *6*, 2020.
[55] J. S. Allen, H. Damasio, T. J. Grabowski, *Am. J. Phys. Anthropol.* **2002**, *118*, 341.
[56] M. Graeser, F. Thieben, P. Szwargulski, F. Werner, N. Gdaniec, M. Boberg, F. Griese, M. Möddel, P. Ludewig, D. van de Ven, O. M. Weber, O. Woywode, B. Gleich, T. Knopp, *Nat. Commun.* **2019**, *10*, 1936.
[57] F. Thieben, F. Foerger, F. Mohn, N. Hackelberg, M. Boberg, J.-P. Scheel, M. Möddel, M. Graeser, T. Knopp, System Characterization of a Human-Sized 3D Real-Time Magnetic Particle Imaging Scanner for Cerebral Applications, *ArXiv:2310.15014 [physics]* **2023**, http://arxiv.org/abs/2310.15014.
[58] Z. Zhuang, B. Bradtmiller, *J. Occup. Environ. Hyg.* **2005**, *2*, 567.
[59] F. Mohn, F. Förger, F. Thieben, M. Möddel, I. Schmale, T. Knopp, M. Graeser, *Rev. Sci. Instrum.* **2024**, *95*, 044701.
[60] F. Fiorillo, G. Bertotti, C. Appino, M. Pasquale, in *Wiley Encyclopedia of Electrical and Electronics Engineering*, John Wiley & Sons, Inc., Hoboken, NJ, USA, **1999**, pp. 1–42, ISBN: 978-0-471-34608-1, https://onlinelibrary.wiley.com/doi/10.1002/047134608X.W4504.pub2.
[61] H. P. Langtangen, A. Logg, *Solving PDEs in Python*, Springer International Publishing, Cham **2016**.
[62] M. Boberg, T. Knopp, M. Möddel, Unique compact representation of magnetic fields using truncated solid harmonic expansions, arXiv: 2302.07591 [physics], **2023**.
[63] K. Svanberg, *Int. J. Numer. Methods Eng.* **1987**, *24*, 359.